

Adjoint-based shape optimization of the microchannels in an inkjet printhead

Petr V. Kungurtsev¹ and Matthew P. Juniper^{1,†}

¹Department of Engineering, University of Cambridge, Cambridge CB2 1PZ, UK

(Received 17 August 2018; revised 4 February 2019; accepted 30 March 2019;
first published online 17 May 2019)

In drop-on-demand inkjet printheads, ink is pumped steadily through small channels, each of which contains an actuator and a nozzle. When an actuator pulses, a droplet is forced through the nozzle, after which acoustic oscillations reverberate within the channel. Manufacturers would like to damp the residual reverberations, without increasing the pressure drop required to drive the steady flow. In this paper we use gradient-based optimization to show that this can be achieved by constricting the channel where the acoustic velocity is largest and enlarging the channel where the acoustic velocity is smallest. This increases the viscothermal dissipation of the acoustics without changing the viscous dissipation of the steady flow. We separate the compressible Navier–Stokes equations into equations for a steady flow with no oscillations and equations for oscillations with no steady flow. We define two objective functions: the viscous dissipation of the steady flow and the dissipation of the oscillations. We then derive the adjoints for both sets of equations, and obtain expressions for the gradient of each objective function with respect to boundary deformations in Hadamard form. We combine these with a gradient-based optimization algorithm, incorporating constraints such as the shapes of the actuator and nozzle. This algorithm quickly converges to a design that has the same viscous dissipation for the steady flow but a 50% larger decay rate for the oscillating flow. We show that this design is nearly optimal. It is a shape that inkjet manufacturers, using physical insight and trial and error, have probably not yet considered. We also show how the adjoint fields provide physical insight into the mechanisms affecting each objective function. The main requirements of this method are that the steady flow Mach number and oscillating flow Mach number are small, and that dissipation is dominated by thermoviscous mechanisms. These requirements are often satisfied in microfluidics, so the method in this paper could be applied to many other applications.

Key words: microfluidics

1. Introduction

Inkjet printers are used extensively in industry to print pictures, patterns and labels onto textiles, ceramics and packaging. Increasingly they are used for 3-D printing and advanced manufacturing (Hoath 2016). This paper concerns one type of

† Email address for correspondence: mpj1001@cam.ac.uk

drop-on-demand printhead. This contains several hundred ink-filled parallel channels, each of which has a piezo-electric actuator on one side and a 20–50 μm nozzle on the opposite side. When a drop is demanded, an electric signal is applied to the actuator. The actuator moves the boundary of the channel by several hundred nanometres, forcing an ink droplet out of the nozzle and onto a moving substrate below. After this droplet formation stage, acoustic oscillations reverberate within the channel, decaying through viscous and thermal dissipation.

In inkjet printers, it is crucial that every nozzle functions identically and that all drops are the same. If a single nozzle stops working, it leaves a straight unprinted line on the substrate. For this reason, ink is flushed continually through the channels. This flushes away any air bubbles and also reduces the chance that any solid impurities become lodged in the nozzle. This, however, comes at a cost: a pump is required to push the ink through the narrow channels. A faster flowrate or more constricted channels require more power, which is dissipated by viscosity in the printhead. In addition, if the characteristics of one droplet depend on the time since the previous droplet, sharp edges become fuzzy. This occurs if the acoustic reverberations from the previous droplet have not died away sufficiently when the next droplet is demanded. This limits the rate at which droplets can be printed to around $100\,000\text{ s}^{-1}$. Manufacturers would like to increase this rate but, to do so, need the reverberations to decay more quickly.

In this paper we consider the reverberation stage of the drop-on-demand process. We ask whether it is possible to change the shape of the printhead's microchannels in order to increase the decay rate of acoustic reverberations while decreasing (or at least maintaining) the pressure drop required to flush ink through the printhead. In both cases, viscous dissipation in the channel is the major damping mechanism. We discover that it is possible to increase one while decreasing the other. The question then arises as to how to find the optimal channel shape. So many shape parameters can be changed that a particularly efficient approach is to use gradient-based optimization algorithms. We define two objective functions: the steady flow viscous dissipation and the oscillating flow decay rate. In this paper we obtain the shape sensitivities of both objective functions and their gradients with respect to all shape parameters using adjoint methods. We then set one objective function to be a constraint.

We reduce the complexity of the problem by splitting the compressible Navier–Stokes equations into equations for a steady flow with no oscillation and equations for an oscillation with no steady flow. This is done by two-parameter low Mach number asymptotic expansion of the equations of motion (Müller 1998; Culick, Heitor & Whitelaw 2012). The oscillating flow equations describe the wave propagation inside the printhead's microchannels (Bogy & Talke 1984). The efficiency of the inkjet devices depends on the natural frequency and the decay rate of the thermoviscous acoustic oscillations (Beltman 1998). In microchannels, the viscous and thermal losses due to the boundary effects are the main damping mechanisms. This also applies to other microfluidic applications, such as hearing aid devices (Christensen 2017), micro electro mechanical systems (MEMS) (Homentcovschi, Murray & Miles 2010; Homentcovschi *et al.* 2014), micro-loudspeakers and microphones (Kampinga, Wijnant & de Boer 2011).

The low Mach number acoustic equations can be simplified for particularly simple geometries (Tijdeman 1975; Moser 1980), or by using boundary-layer analysis (Beltman 1999; Rienstra & Hirschberg 2013; Berggren, Bernland & Noreland 2018). The results of these reduced models, however, are not valid when the thickness of

the boundary layer is of the order of the radii of the surface curvature. Because this paper considers shape deformations without restrictions on the surface curvature, we perform our analysis on the full system of thermoviscous acoustic equations.

Using the adjoint approach, it is possible to obtain the sensitivity of the objective functions to shape modifications. The shape sensitivity of the steady flow viscous dissipation is calculated using results obtained by Schmidt & Schulz (2010). In this paper we derive the adjoint counterpart of the thermoviscous acoustic equations and calculate the natural frequency and decay rate shape sensitivities (e.g. Luchini & Bottaro 2014). The gradient-based optimization is then applied to a two-dimensional (2-D) channel and a generic geometry of the printhead’s microchannels. The main goal of this paper is to describe the method that we use and the physics that it exploits. Constraining the channel to be two-dimensional considerably reduces the computational expense of the problem without altering the most influential aspects of the physics. This is because the longest-lasting residual oscillations are those of the lowest frequency mode, whose frequency is determined mainly by the length of the channel and whose dissipation is predominantly in the boundary layers at the sides of the channel. Our 2-D optimization process changes the height of the channel, increasing this dissipation in influential areas. A 3-D process would also change the width of the channel, but we expect this change to be in the same areas, for the same reasons. The 2-D simulations under-estimate the dissipation because they have two sides, rather than four, but they capture the major shape changes required in both the 2-D and 3-D cases. Nevertheless, our next step is to repeat the calculations for a 3-D geometry and with the large number of extra shape parameters that this will entail.

2. Equations of motion in the low Mach number limit

The motion of a fluid with viscosity, heat conductivity, compressibility and external body forces is governed by the compressible Navier–Stokes equations, which, in conservative form, are governed by:

$$\frac{\partial}{\partial t} \mathbf{q} + \nabla_k (f_k^c(\mathbf{q}) - f_k^v(\mathbf{q}, \nabla \cdot \mathbf{q})) = 0 \quad \text{in } \Omega, \tag{2.1}$$

where ∇_k is the k th component of the spatial derivative $\nabla_k \equiv \partial/\partial x_k$, superscripts c and v refer to convective and viscous components of the equations. The vector of conservative variables, \mathbf{q} , and the fluxes, $f^c(\mathbf{q}), f^v(\mathbf{q})$, are defined by

$$\mathbf{q} \equiv \begin{bmatrix} \rho \\ \rho u_i \\ \rho E \end{bmatrix}, \quad f_k^c(\mathbf{q}) = \begin{bmatrix} \rho u_k \\ \rho u_i u_k + P \delta_{ik} \\ \rho u_k (\rho E + P) \end{bmatrix}, \quad f_k^v(\mathbf{q}) = \begin{bmatrix} 0 \\ \tau_{ki} \\ \tau_{kj} u_j + \kappa \nabla_k T \end{bmatrix}. \tag{2.2a-c}$$

The variables ρ, \mathbf{u}, P, T denote the flow density, velocity vector, pressure and temperature; τ_{ij} is the viscous stress tensor, which is proportional to the dynamic viscosity coefficient μ_{vis}

$$\tau_{ij} = \mu_{vis} \left(\nabla_i u_j + \nabla_j u_i - \frac{2}{3} \delta_{ij} \nabla_k u_k \right), \tag{2.3}$$

and the total energy of the flow E is a sum of the kinetic energy and the static internal energy $e = e(T, P)$:

$$\rho E = \rho e + \frac{\rho u_k u_k}{2}, \tag{2.4}$$

and κ is the thermal conductivity coefficient. We also introduce an equation of state, which relates the pressure, density and temperature:

$$\rho = \rho(P, T). \tag{2.5}$$

2.1. Low Mach number expansion

Equation (2.1) can describe a range of physical phenomena, which is excessive in this case because the system's behaviour is governed to first order by only two phenomena. The first is steady flow in a channel with rigid boundaries, with the inlet velocity of order $\bar{U} = 0.1 \text{ m s}^{-1}$ and $Re \approx 1$. The second is periodic acoustic oscillation, with a small displacement amplitude at the boundary $\Delta \leq 0.1 \text{ }\mu\text{m}$ and a high oscillation frequency $\omega \approx 100 \text{ kHz}$. The characteristic oscillation velocity is of order $\tilde{U} = \omega\Delta \approx 0.01 \text{ m s}^{-1}$.

We choose the ambient state density ρ^b and the speed of sound $(c_s^b)^2 = (\partial P / \partial \rho)_s$ as the reference dimensional density and velocity, and the characteristic domain size L as the reference length. The reference pressure P^b is chosen as a function of density and the speed of sound: $P^b = \rho^b (c_s^b)^2$, and the reference temperature T^b is the ambient temperature.

In this problem, we assume that the local Mach number is small:

$$M \equiv \frac{|u|}{c_s^b} \ll 1. \quad (2.6)$$

The characteristic velocity amplitudes of the steady flow, \bar{U} , and the oscillating flow, \tilde{U} , are also small in comparison to the speed of sound, which allows us to introduce two small parameters: the steady flow Mach number, μ , and the oscillating flow Mach number, ϵ :

$$\mu \equiv \frac{\bar{U}}{c_s^b} \simeq \frac{0.1}{1000} \ll 1, \quad (2.7a)$$

$$\epsilon \equiv \frac{\tilde{U}}{c_s^b} \simeq \frac{0.01}{1000} \ll 1. \quad (2.7b)$$

The oscillating flow time scale differs greatly from the steady flow time scale. The oscillating time scale is $t_{ac} \sim L/c_s$, and the steady flow time scale is $t_{hyd} \sim L/\bar{U} = \mu^{-1} t_{ac} \gg t_{ac}$. This allows us to decouple two phenomena and study them independently. We consider a generic state variable $\psi(\mathbf{x}, t) = (\rho, u_i, P)$. We denote a zero-order state variable by $\psi_0(\mathbf{x}, t)$, as if the steady flow and the oscillating flow were absent, i.e. $\epsilon = \mu = 0$. If there is no external energy and momentum production (by imposed temperature gradients, heat release or body forces), then ψ_0 is uniform in space and constant in time. We then assume that the perturbation $\phi(\mathbf{x}, t)$ of ψ_0 is at least linearly proportional to μ and ϵ , such that:

$$\psi(\mathbf{x}, t) = \psi_0 + \phi(\mathbf{x}, t, \mu, \epsilon). \quad (2.8)$$

We assume that a flow state perturbation related to a particular phenomenon depends solely on the phenomenon's temporal scale, such that $\phi(\mathbf{x}, t)$ becomes a sum of the slow hydrodynamic perturbation $\bar{\phi}(\mathbf{x}, t, \mu)$, labelled the steady flow, and the fast acoustic perturbation $\tilde{\phi}(\mathbf{x}, t, \epsilon)$, labelled the oscillating flow:

$$\phi(\mathbf{x}, t, \mu, \epsilon) = \bar{\phi}(\mathbf{x}, t, \mu) + \tilde{\phi}(\mathbf{x}, t, \epsilon), \quad (2.9a)$$

$$\bar{\phi}(\mathbf{x}, t, \mu) = \frac{1}{T_{ac}} \int_{T_{ac}} \phi(\mathbf{x}, t, \mu, \epsilon) dt. \quad (2.9b)$$

In summary, the generic flow variable $\psi(\mathbf{x}, t)$ consists of the zero-frequency ambient state, ψ_0 , the low-frequency hydrodynamic perturbation $\bar{\phi}(\mathbf{x}, t_{hyd}, \mu)$ and the high-frequency acoustic perturbation $\tilde{\phi}(\mathbf{x}, t_{ac}, \epsilon)$:

$$\psi(\mathbf{x}, t) = \psi_0 + \bar{\phi}(\mathbf{x}, t_{hyd}, \mu) + \tilde{\phi}(\mathbf{x}, t_{ac}, \epsilon). \tag{2.10}$$

We can perform a low Mach number expansion in terms of μ and ϵ because they are both small. The state perturbations $\bar{\phi}(\mathbf{x}, t_{hyd})$ and $\tilde{\phi}(\mathbf{x}, t_{ac})$ independently tend to zero as $\mu \rightarrow 0$ and $\epsilon \rightarrow 0$, so we assume low Mach number decompositions of the form $\bar{\phi}(\mathbf{x}, t_{hyd}) = \|\bar{\phi}\| \sum \mu^k \bar{\phi}^{(k)}(\mathbf{x}, t_{hyd})$ and $\tilde{\phi}(\mathbf{x}, t_{ac}) = \|\tilde{\phi}\| \sum \epsilon^k \tilde{\phi}^{(k)}(\mathbf{x}, t_{ac})$, where $\bar{\phi}^{(k)}$, $\tilde{\phi}^{(k)}$ are the k th-order non-dimensional perturbation shapes, and $\|\bar{\phi}\|$, $\|\tilde{\phi}\|$ are the characteristic dimensional magnitudes of the variables: $\|\bar{\rho}\| = \|\bar{\rho}\| = \rho^b$, $\|\bar{u}\| = \bar{U}$, $\|\bar{u}\| = \bar{U}$, $\|\bar{P}\| = \|\bar{P}\| = P^b$.

We neglect the interaction between the steady flow and the oscillating flow given by the higher-order mixed terms $\sum \mu^n \epsilon^m \phi^{(m+n)}(\mathbf{x}, t_{ac}, t_{hyd})$; $m, n \geq 1$ because ϵ and μ are both small. The expansion of the primal variables is therefore:

$$\rho(x, t) = \rho^b \rho_0 + \rho^b (\mu \bar{\rho}^{(1)} + \epsilon \tilde{\rho}^{(1)}) + O(\mu^2, \epsilon^2, \mu\epsilon), \tag{2.11a}$$

$$u(x, t) = c_s^b (\mu \bar{u}^{(1)} + \epsilon \tilde{u}^{(1)}) + O(\mu^2, \epsilon^2, \mu\epsilon), \tag{2.11b}$$

$$P(x, t) = P^b P_0 + P^b (\mu \bar{P}^{(1)} + \mu^2 \bar{P}^{(2)} + \epsilon \tilde{P}^{(1)}) + O(\mu^3, \epsilon^2, \mu\epsilon). \tag{2.11c}$$

We keep $\mu^2 \bar{P}^{(2)}$ here because the first-order steady flow pressure perturbation $\bar{P}^{(1)}$ does not contribute to the steady flow, being a part of the ambient state, as shown by Müller (1998).

2.2. Zero Mach number limit

Substituting the primal variables expansion (2.11) into (2.1) and (2.5), and collecting the zero-order terms, we obtain:

$$\nabla_i P^{(0)}(x) = 0, \tag{2.12a}$$

$$\nabla_k (\kappa \nabla_k T^{(0)}(x)) = 0, \tag{2.12b}$$

$$\rho^{(0)}(x) = \rho(P^{(0)}, T^{(0)}). \tag{2.12c}$$

The zeroth-order equations describe the ambient state, $\epsilon = \mu = 0$. Equation (2.12a) shows that the ambient pressure P_0 is spatially uniform, and (2.12b) describes the temperature distribution of the ambient state. If all the boundaries have uniform and constant temperature, then the ambient temperature and density are uniform and non-dimensionalized as $T^{(0)}(x) = 1$, $\rho^{(0)}(x) = 1$.

2.3. Low Mach number steady flow

Collecting the first-order terms of μ in the continuity equation and the second-order terms of μ^2 in the momentum equations (2.2) and assuming a Newtonian fluid results in the incompressible Navier–Stokes equation:

$$\nabla_i \bar{u}_i^{(1)} = 0, \tag{2.13a}$$

$$\frac{\partial}{\partial t_{hyd}} \bar{u}_i^{(1)} + (\bar{u}_j^{(1)} \nabla_j) \bar{u}_i^{(1)} + \nabla_i \bar{P}^{(2)} - \frac{1}{Re} \Delta \bar{u}_i^{(1)} = 0. \tag{2.13b}$$

The steady flow pressure perturbation, \bar{P} , balances the nonlinear convective term in the momentum equation, so $\bar{P} = \mu^2 \bar{P}^{(2)} + O(\mu^3)$. Here $\bar{Re} \equiv \rho^b LU_{in}/\mu_{vis}$ is the steady flow Reynolds number.

We supplement the steady flow equations with a prescribed velocity boundary condition at the inlet, Γ_{in} , a no-slip boundary condition on the walls, Γ_w , and a zero stress boundary condition at the outlet, Γ_{out} :

$$\bar{u}_i^{(1)} = U_i \quad \text{on } \Gamma_{in}, \tag{2.14a}$$

$$\bar{u}_i^{(1)} = 0 \quad \text{on } \Gamma_w, \tag{2.14b}$$

$$-\bar{P}^{(2)} n_i + \frac{1}{Re} \frac{\partial \bar{u}_i^{(1)}}{\partial n} = 0 \quad \text{on } \Gamma_{out}. \tag{2.14c}$$

2.4. Low Mach number oscillating flow

Collecting the first-order terms of ϵ , the oscillating flow continuity, momentum and energy equations are governed by:

$$\frac{\partial}{\partial t_{ac}} \tilde{\rho}^{(1)} + \nabla_i \tilde{u}_i^{(1)} = 0, \tag{2.15a}$$

$$\frac{\partial}{\partial t_{ac}} \tilde{u}_i^{(1)} + \nabla_i \tilde{P}^{(1)} = \frac{1}{\bar{Re}} \nabla_j \tilde{\tau}_{ij}^{(1)}, \tag{2.15b}$$

$$\frac{s^b}{c_p} \frac{\partial}{\partial t_{ac}} \tilde{s}^{(1)} = \frac{1}{\bar{Pe}} \Delta \tilde{T}^{(1)}. \tag{2.15c}$$

The Reynolds and Péclet numbers based on the speed of sound are $\bar{Re} \equiv \rho^b L c_s^b / \mu_{vis}$ and $\bar{Pe} \equiv \rho^b L c_s^b c_p / \kappa$. The heat capacity ratio is $\gamma \equiv c_p / c_v$, where c_p and c_v are the specific heats at constant pressure and constant volume, and s^b is the dimensional ambient state entropy. The viscous contribution to the mechanical energy dissipation $\nabla_k (\tilde{\tau}_{kj}^{(1)} \tilde{u}_j^{(1)})$ is absent in (2.15c) because it is second order in ϵ and therefore negligible. We solve the oscillating flow equations in terms of the oscillating flow pressure $\tilde{P}^{(1)}$, velocity $\tilde{u}_i^{(1)}$ and temperature $\tilde{T}^{(1)}$, and express the flow density and entropy as $\tilde{s}^{(1)} = \tilde{s}(\tilde{P}^{(1)}, \tilde{T}^{(1)})$, and $\tilde{\rho}^{(1)} = \tilde{\rho}(\tilde{P}^{(1)}, \tilde{T}^{(1)})$ using the following thermodynamic equalities:

$$s^b \tilde{s}^{(1)} = \left(\frac{\partial S}{\partial P} \right)_T P^b \tilde{P}^{(1)} + \left(\frac{\partial S}{\partial T} \right)_P T^b \tilde{T}^{(1)} = -\frac{\alpha_p}{\rho_b} P^b \tilde{P}^{(1)} + \frac{c_p}{T_b} T^b \tilde{T}^{(1)}, \tag{2.16a}$$

$$\rho^b \tilde{\rho}^{(1)} = \left(\frac{\partial \rho}{\partial P} \right)_T P^b \tilde{P}^{(1)} + \left(\frac{\partial \rho}{\partial T} \right)_P T^b \tilde{T}^{(1)} = \frac{\gamma}{(c_s^b)^2} P^b \tilde{P}^{(1)} - \rho^b \alpha_p T^b \tilde{T}^{(1)}, \tag{2.16b}$$

where $\alpha_p \equiv \rho^b (\partial V / \partial T)_P$ is the volumetric coefficient of thermal expansion. These expressions are substituted into (2.15). For convenience, we redefine the oscillating flow temperature as $\alpha_p T^b \tilde{T}^{(1)} \rightarrow \tilde{T}^{(1)}$, and use the fact that $c_p - c_v = T^b (c_s^b)^2 \alpha_p^2 / \gamma$ to express the continuity (2.15a) and energy (2.15c) equations in terms of pressure and temperature:

$$\frac{\partial}{\partial t_{ac}} (\gamma \tilde{P}^{(1)} - \tilde{T}^{(1)}) + \nabla_i \tilde{u}_i^{(1)} = 0, \tag{2.17a}$$

$$\frac{\partial}{\partial t_{ac}} \left(\frac{\tilde{T}^{(1)}}{\gamma - 1} - \tilde{P}^{(1)} \right) = \frac{1}{\bar{Pe}} \Delta \tilde{T}^{(1)}. \tag{2.17b}$$

The density and entropy variables become

$$\tilde{\rho}^{(1)} \equiv \gamma \tilde{P}^{(1)} - \tilde{T}^{(1)}, \quad \tilde{s}^{(1)} \equiv \frac{\tilde{T}^{(1)}}{\gamma - 1} - \tilde{P}^{(1)}. \quad (2.18a,b)$$

No-slip velocity $\tilde{u}^{(1)} = 0$ and isothermal $\tilde{T}^{(1)} = 0$ boundary conditions induce viscous and thermal boundary layers, which damp the acoustic waves. The thickness of the viscous boundary layer δ_v and the thermal boundary layer δ_T depends on the oscillation frequency (Beltman 1999): $\delta_v(\omega) = \sqrt{\mu_{vis}/(\rho^b \omega)} = \delta_T \sqrt{Pr}$. The non-dimensional viscous and thermal boundary layers thicknesses, $\tilde{\delta}_v(\omega)$, $\tilde{\delta}_T(\omega)$, are:

$$\tilde{\delta}_v^2(\omega) = \frac{\delta_v^2(\omega)}{L^2} = \frac{1}{\tilde{Re}} \frac{\omega_{ac}}{\omega}, \quad \tilde{\delta}_T^2(\omega) = \frac{\delta_T^2(\omega)}{L^2} = \frac{1}{\tilde{Pe}} \frac{\omega_{ac}}{\omega}, \quad (2.19a,b)$$

where $\omega_{ac} = t_{ac}^{-1}$ is the characteristic acoustic frequency. If the oscillation frequency, ω , is similar to or smaller than the acoustic frequency, ω_{ac} , then the viscothermal effects cannot be ignored for general \tilde{Re} , \tilde{Pe} . For an inkjet printhead, the fluid viscosity is of order 10^{-2} Pa s, the speed of sound is 10^3 ms⁻¹ and the channel width is of order 100 μm, which results in $\omega_{ac} = 10$ MHz. At the typical operational frequency of $\omega = 100$ kHz the viscous boundary-layer thickness is then $\tilde{\delta}_v \sim 0.1$. The thermal boundary layer thickness is smaller by a factor of \sqrt{Pr} . For inks used in inkjet printers, with $10 < Pr < 30$ (Seccombe *et al.* 1997) $\tilde{\delta}_T \sim 0.025$.

We perform a modal decomposition of the oscillating flow state vector $\tilde{\mathbf{q}}(x, t) = \hat{\mathbf{q}}(x)e^{st}$. The Laplace transform of (2.15) results in an eigenvalue problem $sB\hat{\mathbf{q}} + A\hat{\mathbf{q}} = 0$ in terms of $\hat{\mathbf{q}} = (\hat{u}_i, \hat{P}, \hat{T})$, where $\hat{\mathbf{q}}$ is the complex eigenfunction, and s is the complex eigenvalue:

$$s \begin{bmatrix} 1 & 0 & 0 \\ 0 & \gamma & -1 \\ 0 & -1 & \frac{1}{\gamma - 1} \end{bmatrix} \begin{bmatrix} \hat{u}_i \\ \hat{P} \\ \hat{T} \end{bmatrix} + \begin{bmatrix} -\frac{1}{\tilde{Re}} \nabla_j \hat{\tau}_{ij} & \nabla_i & 0 \\ \nabla_i & 0 & 0 \\ 0 & 0 & -\frac{\Delta}{(\gamma - 1)\tilde{Pe}} \end{bmatrix} \begin{bmatrix} \hat{u}_i \\ \hat{P} \\ \hat{T} \end{bmatrix} = 0, \quad (2.20a)$$

$$s = \sigma + i\omega, \quad (2.20b)$$

where $-\sigma$ is the decay rate and ω is the angular frequency of the mode. The matrix form of the governing equation for the oscillating flow written in this particular form is Hermitian: $B = B^H$, $A = A^H$.

2.4.1. Boundary conditions

For rigid boundaries we apply a no-slip boundary condition and for open boundaries we apply a stress-free boundary condition:

$$\hat{u}_i = 0 \quad \text{on } \Gamma_{nsl}, \quad (2.21a)$$

$$(-\hat{P}\delta_{ij} + \tilde{Re}^{-1} \hat{\tau}_{ij})n_j = 0 \quad \text{on } \Gamma_{free}. \quad (2.21b)$$

We also apply isothermal and adiabatic boundary conditions for temperature:

$$\hat{T} = 0 \quad \text{on } \Gamma_{iso}, \quad \frac{\partial \hat{T}}{\partial n} = 0 \quad \text{on } \Gamma_{ad}. \quad (2.22a,b)$$

If the boundaries are not rigid, they displace in reaction to the flow on the boundary. For inviscid flow, the boundary impedance, Z , links the pressure to the velocity on the

boundary (Myers 1980). Z is typically frequency dependent: $Z = Z(s)$. For viscous flow, the force at the boundary needs to include the viscous stress, such that the impedance boundary condition is

$$Z\hat{u}_i = (-\hat{P}\delta_{ij} + \tilde{R}e^{-1}\hat{t}_{ij})n_j. \tag{2.23}$$

Here we neither restrict the tangential velocity to be zero nor forbid tangential displacements of the compliant boundary. As $Z \rightarrow 0$, the boundary becomes a free surface, $\hat{\sigma}_{ij}n_j \rightarrow 0$. As $Z \rightarrow \infty$, the boundary becomes a no-slip rigid wall, $\hat{u}_i \rightarrow 0$.

Similarly, the thermal accommodation coefficient $\alpha_w \geq 0$ can be introduced to describe the temperature boundary condition (Carslaw & Jaeger 1986; Beltman 1999),

$$\hat{T} = -\alpha_w \frac{\partial \hat{T}}{\partial n}. \tag{2.24}$$

As $\alpha_w \rightarrow 0$, the boundary becomes isothermal. As $\alpha_w \rightarrow \infty$, the boundary becomes adiabatic.

The domain boundaries can have non-uniform compliance and thermal properties. The boundary impedance and thermal accommodation coefficients are non-uniform frequency-dependent functions, $Z = Z(s)$, $\alpha_w = \alpha_w(s)$ on $\partial\Omega$. In summary, the velocity and temperature boundary conditions can be generalized to Robin boundary conditions (2.23), (2.24), with special cases for rigid and open boundaries:

$$Z = 0 \quad \text{on } \Gamma_{nsl}, \quad Z^{-1} = 0 \quad \text{on } \Gamma_{free}, \tag{2.25a,b}$$

$$\alpha_w = 0 \quad \text{on } \Gamma_{iso}, \quad \alpha_w^{-1} = 0 \quad \text{on } \Gamma_{ad}. \tag{2.25c,d}$$

2.4.2. Energy of the acoustic oscillation

The thermoviscous acoustic problem (2.15) is dissipative, and later we will investigate how and where this dissipation occurs. For this we introduce an energy norm (Chu 1965), \hat{E} , where $*$ denotes the complex conjugate:

$$\hat{E} = \int_{\Omega} \hat{u}_i \hat{u}_i^* + \hat{\rho} \hat{P}^* + \hat{s} \hat{T}^* \, d\mathbf{x}, \tag{2.26}$$

such that the total energy $\tilde{E} = \hat{E}e^{2st}$ decays in time as $e^{2\sigma t}$ (2.20b). We premultiply the oscillating flow governing equation (2.20) by the state vector $\hat{\mathbf{q}}^T$ and integrate it over the volume, $\int_{\Omega} \hat{\mathbf{q}}^T B \hat{\mathbf{q}} + \hat{\mathbf{q}}^T A \hat{\mathbf{q}} = 0$. We integrate the second term by parts once and apply the boundary conditions (2.23), (2.24). The first term is the energy norm, $\int_{\Omega} \hat{\mathbf{q}}^T B \hat{\mathbf{q}} = \hat{E}$, and the second term is the energy dissipation inside the domain and the energy flux through the boundary. We take the real part of this volume integral to express the decay rate of the mode as the sum of volumetric energy dissipation σ_{Ω} and the surface energy transfer $\sigma_{\partial\Omega}$:

$$\begin{aligned} \sigma \equiv \text{Re}(s) &= \frac{1}{\hat{E}} \int_{\Omega} -\frac{1}{\tilde{R}e} \hat{t}_{ij} \nabla_j \hat{u}_i^* - \frac{1}{(\gamma - 1)\tilde{P}e} \|\nabla_i \hat{T}\|^2 \, d\mathbf{x} \\ &+ \frac{1}{\hat{E}} \int_{\partial\Omega} -\frac{\text{Re}(\alpha_w)}{(\gamma - 1)\tilde{P}e} \left\| \frac{\partial \hat{T}}{\partial n} \right\|^2 + \text{Re}(Z) \|\hat{u}_i\|^2 \, ds \\ &\equiv \frac{1}{\hat{E}} \left(\int_{\Omega} \sigma_{\Omega} \, d\mathbf{x} + \int_{\partial\Omega} \sigma_{\partial\Omega} \, ds \right). \end{aligned} \tag{2.27}$$

The volumetric energy dissipation of the acoustic perturbation consists of viscous and thermal dissipation and is always negative, $\sigma_\Omega \leq 0$, while the surface energy transfer of the acoustic perturbation depends on the heat losses through the boundary and the work done by or on the fluid at the boundary. For the rigid and open boundary conditions (2.25) the surface energy transfer vanishes.

3. Shape sensitivities

3.1. Shape gradients in Hadamard form

We consider a governing equation $\mathcal{R}(q, \mathbf{a}) = 0$ satisfied over a domain Ω , with solution q for parameters \mathbf{a} . We define an objective function $J(q, \Omega, \mathbf{a})$. The gradient of J with respect to a parameter variation, $\delta\mathbf{a}$, at $\mathbf{a} = \mathbf{a}_0$, $q_0 = q(\mathbf{a}_0)$, $\Omega_0 = \Omega(\mathbf{a}_0)$, is denoted with a square bracket $J'[\delta\mathbf{a}]$:

$$J'(q_0, \Omega_0, \mathbf{a}_0)[\delta\mathbf{a}] = \lim_{\xi \rightarrow 0^+} \frac{J(q(\mathbf{a}_0 + \xi\delta\mathbf{a}), \Omega(\mathbf{a}_0 + \xi\delta\mathbf{a})) - J_0}{\xi}. \tag{3.1}$$

In shape optimization, the parameters \mathbf{a} also determine the domain boundary $\Gamma = \partial\Omega$. In two dimensions, a displacement field $V : \mathbb{R}^2 \rightarrow \mathbb{R}^2$ defined in Ω represents the domain deformation, and ξ is the displacement amplitude. We denote the perturbed domain as Ω_ξ , and q_ξ as the corresponding perturbed flow state. A perturbed boundary $\Gamma_\xi = \partial\Omega_\xi$ is given by

$$\Gamma_\xi = \Gamma + \xi V(\mathbf{x}) \quad \text{for } \mathbf{x} \in \Gamma. \tag{3.2}$$

If the domain boundary Γ is sufficiently smooth, any tangential displacement only changes the boundary parametrization but not the actual shape. Therefore the boundary displacements in the direction of V and its normal component $(V \cdot \mathbf{n})\mathbf{n}$ are equivalent, where \mathbf{n} is the boundary unit normal vector.

The shape derivative of a general boundary condition independent of the geometry, in particular independent of the surface normal, can be calculated as follows. Given a boundary condition $\mathbf{g}(q_0) = g_0$ on the unperturbed boundary Γ_0 , the perturbed boundary condition $\mathbf{g}(q_\xi) = g_\xi$ on Γ_ξ can be linearized around Γ_0 for a small shape deformation with magnitude $\xi \ll 1$. We expand the perturbed solution as

$$\begin{aligned} q_\xi(\Gamma_\xi) &= (1 + \xi(V \cdot \nabla))q_\xi(\Gamma_0) + O(\xi^2) = (1 + \xi(V \cdot \nabla))(q_0(\Gamma_0) + \xi q'_0[V](\Gamma_0)) + O(\xi^2) \\ &= q_0(\Gamma_0) + \xi q'_0[V](\Gamma_0) + \xi(V \cdot \nabla)q_0(\Gamma_0) + O(\xi^2), \end{aligned} \tag{3.3}$$

such that the total derivative of the solution with respect to the shape perturbation V is $dq[V] \equiv q'_0[V](\Gamma_0) + (V \cdot \nabla)q_\xi(\Gamma_0)$ and $q'_0[V]$ is the local shape derivative. The linearization of the boundary condition is

$$\mathbf{g}(q_\xi(\Gamma_\xi)) = \mathbf{g}(q_0 + \xi dq[V]) = \mathbf{g}(q_0, \Gamma_0) + \xi \left(\frac{\partial \mathbf{g}}{\partial q} \Big|_0 (q'_0[V] + (V \cdot \nabla)q_0) \right) + O(\xi^2), \tag{3.4}$$

where the subscript $|_0$ indicates the value at $q = q_0$, $\Gamma = \Gamma_0$. The term $(\partial \mathbf{g} / \partial q)|_0 q'_0[V]$ represents the boundary condition of the first-order solution's response to shape deformation on the unperturbed boundary. It can be expressed in terms of the initial solution q_0 as

$$\frac{\partial \mathbf{g}}{\partial q} \Big|_0 q'_0[V] = \lim_{\xi \rightarrow 0^+} \frac{g_{b,\xi} - g_{b,0}}{\xi} - \frac{\partial \mathbf{g}}{\partial q} \Big|_0 (V \cdot \nabla)q_0 = (V \cdot \nabla)g_{b,0} - \frac{\partial \mathbf{g}}{\partial q} \Big|_0 (V \cdot \nabla)q_0. \tag{3.5}$$

A shape derivative $J'(\Omega)[V]$ can be written in Hadamard form as a scalar product of a sensitivity functional $G(q, q^+)$ and the normal component of the deformation field V , where q^+ is the adjoint state:

$$J'[V] = \int_{\Gamma_0} (V \cdot \mathbf{n}) G(q, q^+) \, ds. \tag{3.6}$$

In the following sections, we discuss the choice of the objective functions for the steady and the oscillating flows, construct the adjoint states and derive the corresponding sensitivity functionals.

3.2. Steady flow shape sensitivity

For the steady flow, we wish to minimize the viscous dissipation, J_{vd} , in the domain:

$$J_{vd}(\bar{u}, \Omega) = \int_{\Omega} \frac{1}{Re} (\nabla_j \bar{u}_i)^2 \, d\mathbf{x}, \tag{3.7}$$

where \bar{u} satisfies the momentum equation and the divergence-free condition given by (2.13), (2.14). As discussed by Schmidt & Schulz (2010), the viscous dissipation sensitivity functional G_{vd} for a shape displacement defined on a no-slip surface is

$$G_{vd}(\bar{u}_i, \lambda_i) = \frac{1}{Re} \frac{\partial \bar{u}_i}{\partial n} \frac{\partial (\lambda_i - \bar{u}_i)}{\partial n}, \tag{3.8}$$

where λ_i and λ_p are the adjoint velocity and pressure states satisfying

$$\bar{u}_j \nabla_j \lambda_i + \bar{u}_j \nabla_i \lambda_j + \nu \Delta \lambda_i + \nabla_i \lambda_p = \frac{2}{Re} \Delta \bar{u}_i, \tag{3.9a}$$

$$\nabla_i \lambda_i = 0, \quad \text{in } \Omega, \tag{3.9b}$$

$$\lambda_i = 0 \quad \text{on } \Gamma_{in} \cup \Gamma_w, \tag{3.9c}$$

$$\lambda_i \bar{u}_j n_j + \lambda_j \bar{u}_i n_i + \nu \frac{\partial \lambda_i}{\partial n} + \lambda_p n_i = \frac{2}{Re} \frac{\partial \bar{u}_i}{\partial n} \quad \text{on } \Gamma_{out}. \tag{3.9d}$$

The right-hand side source terms of the adjoint equations and boundary conditions depend on the choice of the objective function, while the left-hand sides are governed only by the direct steady flow formulation.

3.3. Oscillating flow shape sensitivity

For the oscillating flow we wish to control the decay rate and frequency (Luchini & Bottaro 2014), so the objective function is the complex natural frequency, s , of the thermoviscous acoustic flow (2.20):

$$J_s = s. \tag{3.10}$$

We introduce an adjoint state vector $\mathbf{q}^+ = (P^+, u_i^+, T^+)$ containing the adjoint pressure, velocity and temperature variables. Taking the inner product of the direct equations and the corresponding adjoint variables, we construct a Lagrangian of the system (Gunzburger 2002),

$$\mathcal{L} = s - \langle \mathbf{q}^+, sB\hat{\mathbf{q}} + A\hat{\mathbf{q}} \rangle. \tag{3.11}$$

The optimality condition sets any first Lagrangian variation to zero. Variation with respect to the adjoint and direct variables gives the direct and the adjoint state equations, respectively. As discussed in § A.1, the adjoint and the direct states of the thermoviscous acoustic problem are related by $P^+ = \hat{P}^*$, $u_i^+ = -\hat{u}_i^*$, $T^+ = \hat{T}^*$, subject to the normalization condition:

$$1 = \langle u_i^+, \hat{u}_i \rangle + \langle P^+, \gamma \hat{P} - \hat{T} \rangle + \left\langle T^+, \frac{\hat{T}}{\gamma - 1} - \hat{P} \right\rangle + \left\{ u_i^+, \frac{\partial Z}{\partial s} \hat{u}_i \right\} - \left\{ \frac{\partial T^+}{\partial n}, \frac{(\partial \alpha_w / \partial s)}{(\gamma - 1) \tilde{P}e} \frac{\partial \hat{T}}{\partial n} \right\}, \tag{3.12}$$

where we define the volume inner product $\langle a^+, b \rangle = \int_{\Omega} (a^+)^* b \, d\mathbf{x}$ (A 3a) and the surface inner product $\{a^+, b\} = \int_{\partial\Omega} (a^+)^* b \, ds$ (A 3b).

For a shape deformation normal to a boundary, the oscillating flow eigenvalue sensitivity G_s consists of the surface stress and the thermal terms, $G_s = G_s^{str} + G_s^{th}$ (derived in § A.2). Given that the direct and adjoint states are identical up to the sign of the velocity term, the sensitivity functionals are:

$$\left. \begin{aligned} G_s^{str} &= - \left(2 \frac{\partial \hat{u}_i}{\partial n} n_j \hat{\sigma}_{ij} + \kappa \hat{u}_i \hat{\sigma}_{ij} n_j - \nabla_j (\hat{u}_i \hat{\sigma}_{ij}) \right), \\ G_s^{th} &= 2 \frac{\partial \hat{T}}{\partial n} \hat{q}_n + \kappa \hat{T} \hat{q}_n - \nabla_j (\hat{T} \hat{q}_j), \end{aligned} \right\} \tag{3.13}$$

where $\hat{q}_i \equiv ((\gamma - 1) \tilde{P}e)^{-1} \nabla_i \hat{T}$ is the boundary heat flux, and $\hat{q}_n = (\hat{q} \cdot \mathbf{n})$ is its normal component. The viscous and the thermal sensitivity functionals have equivalent structure in terms of the $(\hat{u}_i, \hat{\sigma}_{ij})$ and (\hat{T}, \hat{q}_i) pairs.

On the no-slip and stress-free boundaries, the viscous sensitivity functional simplifies to

$$G_{s,nsl}^{str} = - \frac{\partial \hat{u}_i}{\partial n} n_j \hat{\sigma}_{ij}, \tag{3.14a}$$

$$G_{s,free}^{str} = \nabla_j (\hat{u}_i \hat{\sigma}_{ij}), \tag{3.14b}$$

and on the isothermal and adiabatic boundaries, the thermal sensitivity functional simplifies to

$$G_{s,iso}^{th} = \frac{\partial \hat{T}}{\partial n} \hat{q}_n, \tag{3.15a}$$

$$G_{s,ad}^{th} = - \nabla_j (\hat{T} \hat{q}_j). \tag{3.15b}$$

4. Shape optimization in a 2-D channel

4.1. Numerical methods

4.1.1. Optimization domain

We start with a flow in a two-dimensional uniform-width channel, defined as

$$\Omega_0 = \{(x, y) \in \mathbb{R}^2 \mid [0, 1] \times [0, 0.1]\}, \tag{4.1}$$

with inlet and outlet boundaries

$$\Gamma_{in,0} = \{(x, y) \in \mathbb{R}^2 \mid x = 0\}, \quad (4.2a)$$

$$\Gamma_{out,0} = \{(x, y) \in \mathbb{R}^2 \mid x = 1\}, \quad (4.2b)$$

and no-slip boundaries $\Gamma_{w,0} = \partial\Omega_0 \setminus (\Gamma_{in,0} \cup \Gamma_{out,0})$. For the oscillating flow, the stress-free boundary is $\Gamma_{free,0} = \Gamma_{in,0} \cup \Gamma_{out,0}$.

The boundary $\Gamma_{w,0}$ is to be optimized by modifying the no-slip boundaries, while fixing the inlet and the outlet. If equivalent boundary displacement fields are applied to the top and the bottom no-slip surfaces then the steady flow and the oscillating flow boundary sensitivities and the shape gradients remain symmetric. Therefore we may consider deformation of only the top boundary.

In this study, we parametrize the boundary with a set of N control points $\{a^k \in \mathbb{R}^2 \mid k = 1 \dots N\}$ defining the third-order rational uniform B-spline curve. This provides a smooth surface of class C^2 for which parametric sensitivities can be calculated (Samareh 2001). Boundary displacement fields, V^k , are, by definition, the boundary shape sensitivities to the control point positions,

$$V^k = \frac{\partial \Gamma_w}{\partial a^k}, \quad (4.3)$$

which implies that the objective function gradient with respect to the displacement field $J'[V^k]$ transforms to the sensitivity with respect to the control parameters, $J'[a^k]$. As the positions of the control points are moved in the gradient direction, the domain is updated and the computational mesh is rebuilt.

We parametrize the top boundary of the initial rectangular domain with 11 control points, $a_i = (i/10, 0.1)$, $i = 0 \dots 10$, spaced uniformly at intervals of 0.1. The first and last points are kept at their initial positions so that the inlet and outlet boundaries are fixed and the channel's length remains equal to 1.

4.1.2. Numerical discretization

We use a finite element method for spatial discretization. The direct and adjoint formulations of the steady flow problem and the direct formulation of the oscillating flow problem are first written in a variational form and then discretized using the Fenics finite elements solver (Logg, Mardal & Wells 2012) on a mesh of triangular elements generated by Gmsh (Geuzaine & Remacle 2009). The velocity and pressure fields (\tilde{u}_i, \tilde{P}) (2.13), (2.14) and the adjoint fields (λ_i, λ_p) (3.9) for the steady flow are discretized using Taylor–Hood (P_2, P_1) elements. The acoustic perturbation field $(\tilde{P}, \tilde{u}_i, \tilde{T})$ (2.20) is discretized using (P_1, P_2, P_2) elements (see Kampinga, Wijnant & de Boer 2010). The resulting discrete sparse matrices are inverted by a direct lower–upper (LU) solver using a multifrontal massively parallel sparse direct solver (MUMPS).

For the steady flow problem, the Dirichlet-type boundary conditions are set up strongly for each boundary degree of freedom and the outlet boundary condition is enforced weakly. The nonlinear direct flow is solved using a Newton iterative method. The steady flow inlet velocity profile is parabolic. The oscillating flow problem is a generalized eigenvalue problem and is solved with a shift-invert method from an initial guess.

The oscillating flow viscous and thermal boundary layers are resolved using triangular elements. We apply the goal-oriented adjoint-based error control technique (Rognes & Logg 2013) for the automated adaptive mesh refinement. The goal functional in our case is the target eigenvalue.

4.1.3. Constrained gradient optimization

Our goals are to decrease the steady flow viscous dissipation and make the oscillation's decay rate, $-\sigma$, more negative. There is a trade-off between these goals, so here we set the steady flow dissipation as an inequality constraint and minimize $\text{Re}(s)$.

$$\min_{\Omega} \quad \text{Re}(s) \quad (4.4a)$$

$$\text{subject to} \quad J_{vd} \leq J_{vd}^0 \quad (4.4b)$$

$$\text{and} \quad \text{state equations (2.13), (2.20)}. \quad (4.4c)$$

In §A.1 we derive shape gradients in Hadamard form of both the objective function and the constraint with respect to an arbitrary boundary displacement V . The parameter-based approach restricts the number of possible boundary deformations to the number of control parameters. Essentially, a parametrization projects the function space of the admissible shape deformations onto a lower-dimensional subspace, which allows us to operate with the vector representation of shape gradients instead of the continuous boundary sensitivities.

We can estimate the optimality of a shape (but not the parametrization) by considering the scalar product of the objective shape sensitivity, G , with the constraint shape sensitivity, G' . The surface inner product $\{G, G'\}$ (A3) and the surface norm $\|G\|_r^2 = \{G, G\}$ form the optimality coefficient α :

$$\alpha = \frac{\{G, G'\}}{\|G\|_r \|G'\|_r} \geq -1. \quad (4.5)$$

The optimality coefficient indicates the cosine of the angle between the objective function shape sensitivity and the constraint shape sensitivity, such that $\alpha = -1$ implies that they point in opposite directions and the system has reached its local optimum. In the case of N optimization parameters, a sensitivity functional is realized on a shape deformation subspace, spanned by V^k , $k = 1 \dots N$. The discrete gradient vector $\mathbf{g} \in \mathbb{R}^N$ is defined as $\mathbf{g}_k = \{V^k, G\}$, and the parametric optimality coefficient α_p is:

$$\alpha_p = \frac{\mathbf{g}^T \mathbf{g}'}{\|\mathbf{g}\| \cdot \|\mathbf{g}'\|} \leq \alpha. \quad (4.6)$$

In the parameter-based optimization, $\alpha_p = -1$ implies that the local optimum has been reached within the choice of parametrization.

The optimization algorithm for the problem (4.4) is based on the method of moving asymptotes (Svanberg 1987). The objective and the constraint values and their gradients are calculated by (i) solving the steady flow (2.13) and the oscillating eigenvalue (2.20) problems, (ii) finding the adjoint steady flow (3.9) and oscillating flow (3.12) states, (iii) calculating the boundary sensitivities G_{vd} , G_s using (3.8) and (3.13), and computing the objective and constraint gradients with respect to the boundary control points $s'[a_k] = \{V^k, G_s\}$, $J'_{vd}[a_k] = \{V^k, G_{vd}\}$. We use $\varepsilon_p = \alpha_p + 1$ as a tolerance criteria for the optimization process.

4.2. Optimization results

4.2.1. Initial domain

The steady flow is computed in the initially flat channel (4.1) at $\overline{Re} = 0.1$ with a parabolic inflow velocity profile. In the unaltered domain this results in the

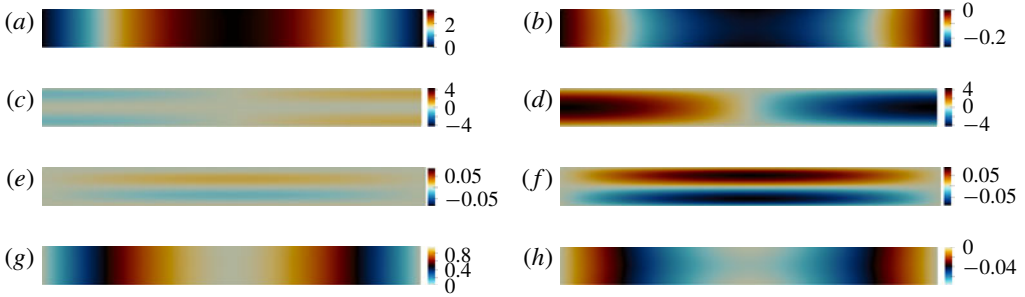


FIGURE 1. (Colour online) First natural mode of the oscillating flow in a flat channel at $\tilde{Re} = 1000$. (a–h) Pressure \hat{P} , longitudinal \hat{u}_x and transverse \hat{u}_y velocity components, and temperature \hat{T} mode shapes; real (a,c,e,g) and imaginary (b,d,f,h) parts.

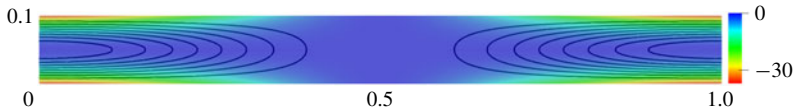


FIGURE 2. (Colour online) Spatial distribution of the decay rate production σ_Ω in a flat channel. Black lines correspond to the oscillating flow velocity magnitude isolines $\hat{u} = \text{const}$.

Poiseuille flow solution, and the corresponding viscous dissipation value J_{vd}^0 is taken as a reference. For the oscillating flow at $\tilde{Re} = 1000$, we choose the smallest non-zero-frequency natural mode as the target mode, with $s_0 = -0.555 + 2.81i$. Figure 1 shows the real and imaginary parts of the mode shape, normalized by (3.12). The pressure gradient $\partial_x \hat{P}$ and the longitudinal velocity \hat{u}_x are highest on the stress-free open end boundaries at $x = 0, x = 1$. As indicated in figure 2, the regions with the highest contribution to the decay rate σ_Ω are the no-slip wall regions close to the open ends, where the velocity magnitude isolines converge and therefore the transverse velocity gradient is the largest. For the initial channel configuration, $\alpha_p = -0.7$.

The steady flow state in the unperturbed channel is independent of the longitudinal coordinate x so the viscous dissipation shape sensitivity $G_{vd}(\bar{u}_i, \lambda_i)$ is constant along the no-slip walls (figure 3). Here, and later, G_{vd} is normalized by the viscous dissipation value J_{vd}^0 in the starting geometry configuration. The shape sensitivity G_{vd} is always negative, so any boundary displacement resulting in contraction of the channel’s width leads to growth of viscous dissipation. The complex eigenvalue shape sensitivity $G_s(\hat{P}, \hat{u}_i, \hat{T})$ is not uniform; the real part $\text{Re}(G_s)$ is almost zero in the middle part of the boundary and grows towards the channel’s open ends where the decay rate production is highest, as shown previously. As for viscous dissipation, any shape deformation directed inwards ($V \cdot \mathbf{n} < 0$) leads to an increase in the decay rate magnitude.

As indicated in figure 3, the decay rate is less sensitive to shape modifications in the middle region of the channel at $0.3 \leq x \leq 0.7$, and has higher sensitivity on the outer region. We expect therefore, that the channel will expand in the middle and shrink around the free boundaries to increase the decay rate while keeping the steady flow viscous dissipation constant. This is also what we expect on physical grounds: the channels will constrict where the acoustic velocity is greater.

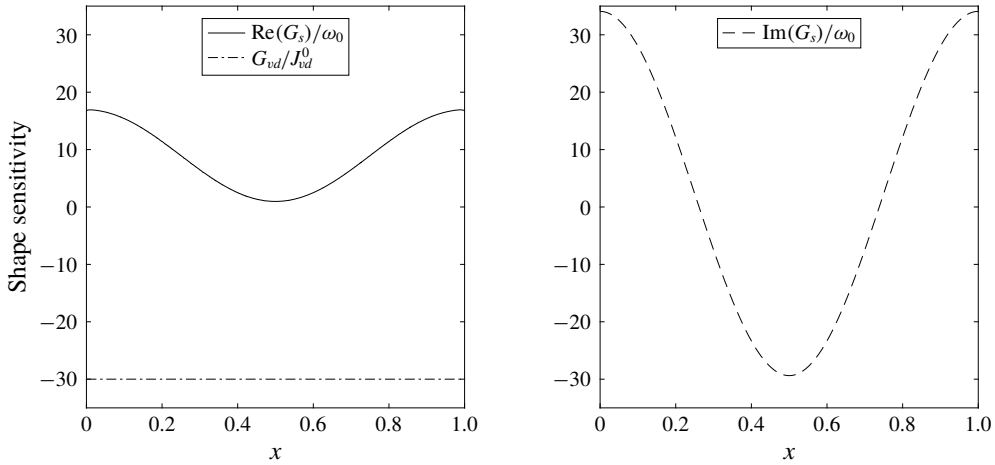


FIGURE 3. Shape sensitivity distribution along the flat channel top boundary for the decay rate $\text{Re}(G_s)$ (solid line) and frequency $\text{Im}(G_s)$ (dashed line) of the first oscillating mode, and the steady flow viscous dissipation shape sensitivity G_{vd}/J_0 normalized by viscous dissipation inside the channel (dotted line).

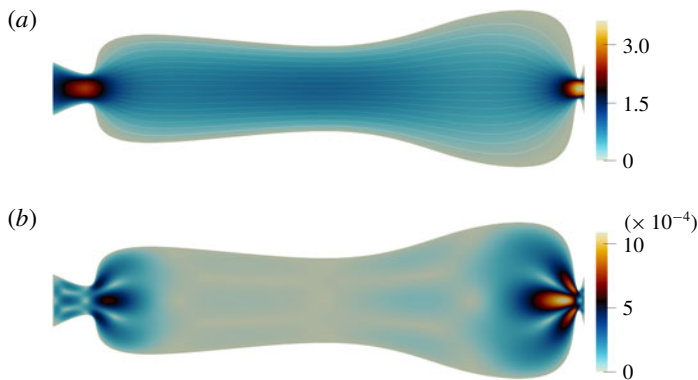


FIGURE 4. (Colour online) Steady flow in the optimized channel at $\overline{Re} = 0.1$. (a) The direct steady flow $|\bar{u}|$ velocity magnitude, with the streamlines indicated (solid lines). (b) The adjoint steady flow $|\lambda|$ velocity magnitude.

4.2.2. Optimized domain

The optimized configuration is found in 20 iterations and has the optimality coefficient (4.5) of $\alpha_p = -0.98$. The first eigenmode in the optimized channel is $s = -1.31 + 1.68i$. In comparison to the initial solution, the decay rate objective function changes by almost 140%, and the frequency (which is unconstrained) decreases by 40%. The total area almost doubles and the channel's shape loses symmetry around the $x = 0.5$ vertical plane, while remaining symmetric in the horizontal plane. The channel constricts near $x = 0.07$ and $x = 0.99$, and the middle part of the channel expands, as expected.

Figure 4 shows the steady flow (a) and the adjoint flow (b) velocity magnitude \bar{u} and λ for the optimized channel. The lines correspond to the steady flow streamlines. The no-slip boundaries are smooth and the flow remains attached to the walls with

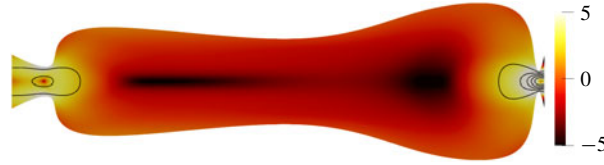


FIGURE 5. (Colour online) Spatial distribution of the absolute value of the decay rate production in the optimized channel (on a logarithmic scale), $\ln(-\sigma_\Omega)$. Black lines correspond to the oscillating flow velocity magnitude isolines $\hat{u} = \text{const}$.

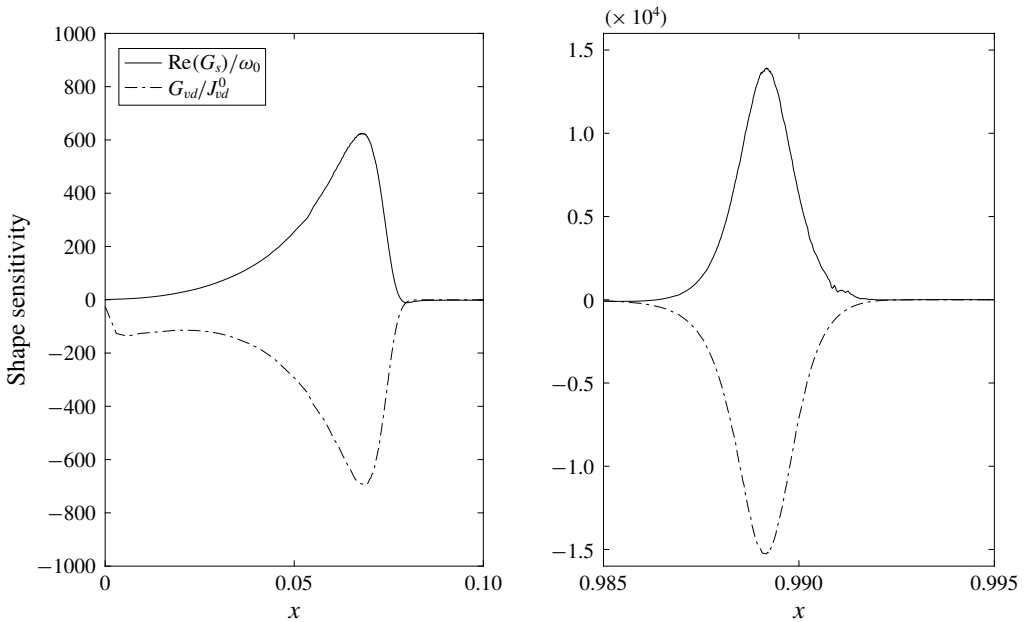


FIGURE 6. The decay rate shape sensitivity distribution (solid line) of the first oscillating mode in the optimized channel, and the steady flow viscous dissipation sensitivity (dotted line) normalized by viscous dissipation inside the channel.

no recirculation zones. Viscous dissipation in the optimized channel is the same as in the initial channel.

The steady flow velocity amplitude and velocity gradients as well as the adjoint velocity are highest in the constricted areas. This makes the constricted regions much more sensitive to shape changes than the expanded part, where the adjoint velocity magnitude is almost zero.

The decay rate production is initially located in the corner regions of the uniform-width channel. When the boundaries shift, this region shifts inside the channel towards the constrictions, as indicated in figure 5. The decay rate production strongly concentrates in the narrow parts of the channel, with the maximum at $x = 0.99$ more than 10 000 times higher than the average value. It is almost zero between the constrictions.

Figure 6 illustrates the viscous dissipation G_{vd}/J_{vd}^0 (dash-dotted line) and the decay rate $\text{Re}(G_s)/\omega_0$ (solid line) boundary sensitivities as functions of the longitudinal

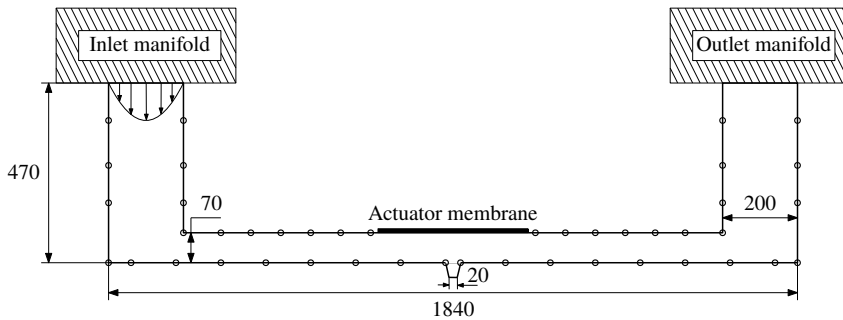


FIGURE 7. A 2-D generic printhead geometry with a piezo-electric actuator. The channel is connected to the ink supply manifolds via the inlet and outlet boundaries. Circles denote the B-spline boundary control points. All sizes are in μm .

coordinate along the top boundary in the optimized channel. Both sensitivities reach their extreme values in the constricted areas and are much smaller in the intermediate region. They are almost equal and opposite to each other, showing that the design is almost optimal. Further improvements can still be made, for instance, by boundary re-parametrization or by introducing additional control points. However, this simple problem has achieved its purpose by showing that the optimization procedure can indeed increase acoustic dissipation while keeping the steady flow dissipation constant.

5. Shape optimization for a 2-D generic inkjet printhead

5.1. Generic geometry and shape parametrization

Figure 7 shows a 2-D generic inkjet printhead chamber, which consists of a vertical inlet and outlet, connected to ink manifolds, and a horizontal main channel. The manifold cross-sections are much larger than the printhead cross-section. A $30\ \mu\text{m}$ long conical printing nozzle, which has a $20\ \mu\text{m}$ outer diameter and a taper of 8° , is located in the middle of the printhead. A flat piezo-electric membrane is located on the top boundary opposite the nozzle. In three dimensions, the channel has a depth of $60\ \mu\text{m}$ into the page. For this study, we approximate the channel to be uniform in that direction and examine only 2-D deformations, as in § 4.2. We aim to increase the decay rate of the oscillating flow while keeping the steady flow viscous dissipation constant.

We parametrize the printhead walls by third-order B-splines with the control points indicated in figure 7. The inlet and the outlet points are fixed. The nozzle shape cannot change but it can move in the vertical direction. The bottom wall cannot extend below the nozzle tip.

We choose a characteristic length $L = 100\ \mu\text{m}$. The steady flow Reynolds number is $\overline{Re} = 0.066$ and the Reynolds number based on the speed of sound is $\tilde{Re} = 6000$. The steady flow Mach number is $\mu = 10^{-4}$ and the oscillating flow Mach number is $\epsilon = 10^{-5}$. For the steady flow, the inlet has a fixed parabolic velocity profile, the outlet is an open end with stress-free boundary condition (2.14c) and the walls are no-slip boundaries and the nozzle exit is modelled as a no-slip boundary because there is no flow through it. For the acoustic flow, the walls are adiabatic no slip, and the open boundaries, including the nozzle exit, are stress free and isothermal. In this study we neglect the surface tension at the nozzle exit.

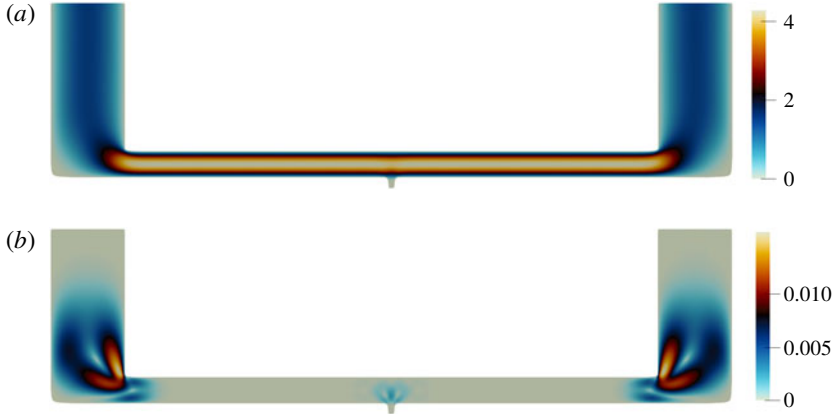


FIGURE 8. (Colour online) The direct velocity magnitude \bar{u} (a) and the adjoint velocity magnitude λ (b) of the steady flow in the initial printhead channel at $\bar{Re} = 0.066$.

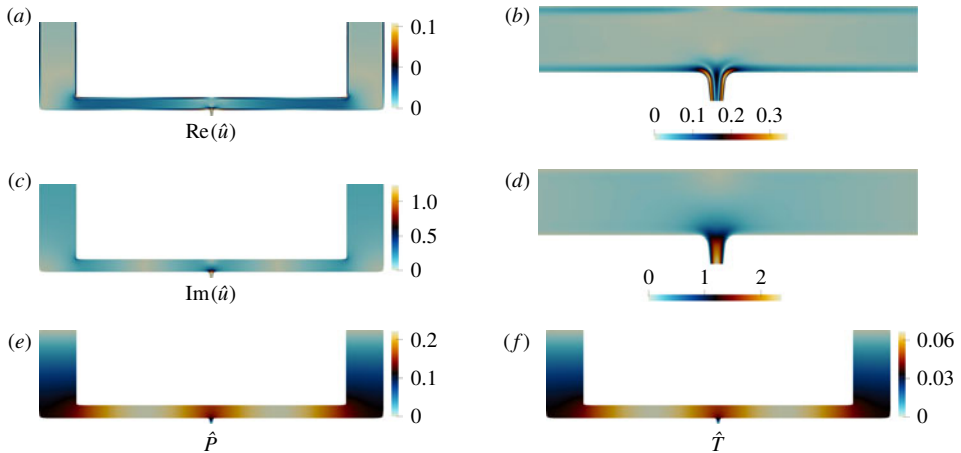


FIGURE 9. (Colour online) The first natural mode of the oscillating flow in the initial printhead geometry at $\bar{Re} = 6000$. (a,b) The magnitude of the velocity mode real part $\text{Re}(\hat{u})$ in the entire domain (a) and near the nozzle (b); (c,d) the magnitude of the velocity mode imaginary part $\text{Im}(\hat{u})$; (e) pressure mode \hat{P} ; and (f) temperature mode \hat{T} .

Figure 8 shows the steady flow direct \bar{u} and adjoint λ velocity magnitude in the initial geometry. The largest direct velocity magnitude is in the narrow horizontal channel. The adjoint velocity has highest value near the sharp corners at the channel entrance and the nozzle. These regions have the greatest influence on the steady flow viscous dissipation.

The frequency of the first natural mode is $\text{Im}(s_1/2\pi) = \omega/2\pi = 0.342$ MHz, and the decay rate is $\text{Re}(s_1/2\pi) = \sigma/2\pi = 0.0171$ MHz. Figure 9 shows the mode shape, normalized by (3.12). The pressure and the temperature modes are zero on the stress-free boundaries and have antinodes in the middle of the channel. Since the walls are adiabatic, the thermal boundary layer is absent and the pressure and temperature gradients are tangential to the boundaries. The velocity magnitude is highest near the nozzle, as shown in figure 9, where the viscous boundary layers overlap. The decay

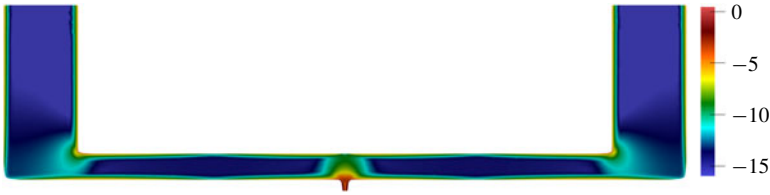


FIGURE 10. (Colour online) Spatial distribution of the absolute value of the decay rate production in the initial printhead channel (on a logarithmic scale), $\ln(-\sigma_\Omega)$.

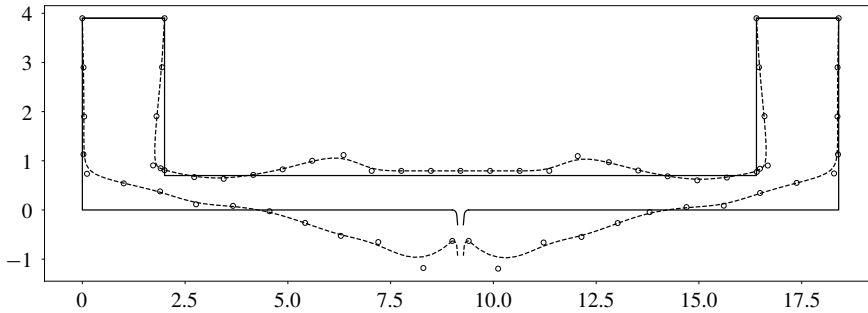


FIGURE 11. The initial (solid lines) and the optimized (dashed lines) printhead geometry. The inlet and the outlet boundaries remain fixed. The piezo-electric membrane and nozzle parts can move up and down but cannot change shape.

rate production is shown in figure 10. It is concentrated in the nozzle region of the initial printhead configuration, in the viscous boundary layers along the no-slip walls, and around the corners.

The parametric optimality coefficient for the initial printhead design is $\alpha_p = 0.017$, which implies that the decay rate and the viscous dissipation gradient vectors are almost orthogonal. Therefore we expect to be able to obtain a noticeable improvement in the objective function.

5.2. Optimization

In this section we use the optimization algorithm in § 4.1.3 to update the control points until the relative improvement falls below the tolerance level of $\varepsilon_p \leq 0.1$. The optimized domain is shown in figure 11. The channel constricts near the corners of the top boundary, where the decay rate production had a local maximum. These constrictions increase the steady flow viscous dissipation there, but the central part of the channel expands to compensate. The new frequency of the first natural mode is $\text{Im}(s_1/2\pi) = \omega/2\pi = 0.264$ MHz, and the decay rate increases to $\text{Re}(s_1/2\pi) = \sigma/2\pi = 0.0257$ MHz, which is over 50% higher than before. The steady flow viscous dissipation is the same as in the initial printhead. The parametric optimality coefficient of the optimized shape is $\alpha_p = -0.94$, showing that it is nearly optimal.

Figure 12 shows the spatial distribution of the decay rate production $\ln(-\sigma_\Omega)$ inside the optimized domain. The viscous boundary layers overlap in the narrow parts of the channel, resulting in higher acoustic energy dissipation there. The highest amplitudes

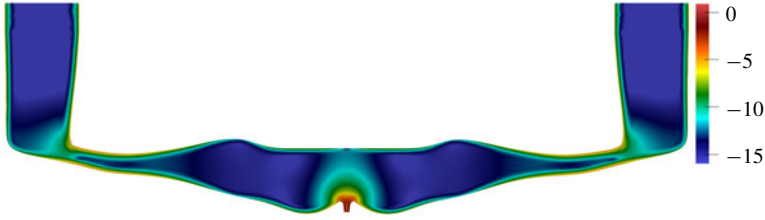


FIGURE 12. (Colour online) Spatial distribution of the decay rate production absolute value in the optimized printhead channel (on a logarithmic scale), $\ln(-\sigma_\Omega)$.

of decay rate production are around the nozzle. This shows that changes to the nozzle geometry are particularly influential.

6. Conclusions

In this paper we perform constrained gradient-based shape optimization of a microchannel in an inkjet print head. Two Mach numbers are formed: one based on the steady flow and the other on the oscillating flow. Both Mach numbers are small, which allows us to separate the flow into (i) a steady flow with no oscillations (2.13) and (ii) oscillations with no steady flow (2.15). We then seek to control two objective functions by changing the shape of the boundaries. The objective functions are (i) the viscous dissipation of the first flow and (ii) a complex number that encapsulates the growth/decay rate and frequency of the second flow. We obtain expressions for the derivatives of the above objective functions with respect to boundary deformations in Hadamard form by deriving the adjoint equations for both flows.

These equations are general and could be used in many ways. We start by showing how they can be combined with an optimization algorithm in order to increase the viscous and thermal dissipation of oscillations in a channel without changing the viscous dissipation of the steady flow in the channel. This works by constricting the channel where the acoustic velocity is largest and enlarging the channel where the acoustic velocity is smallest. This result is straightforward and could have been obtained using physical intuition.

We then apply this technique to the same problem in a 2-D generic inkjet printhead. The printhead manufacturer would like to increase the decay rate of residual oscillations after a drop has been ejected, without changing the pressure drop required to continually flush ink through the head. Starting from a generic design and incorporating constraints such as the sizes of the nozzle and piezo-electric actuator, the algorithm converges to a design with a 50% larger decay rate, but the same pressure drop, which we show to be nearly optimal. The final shape is not straightforward and would have been difficult to achieve through physical insight or trial and error. It could be improved further by adapting the parameters that describe the shape, but in this case the improvement would be small.

In this paper we derive and demonstrate a new way to optimize the shapes of channels that contain thermoviscous oscillating flows with (or without) steady flow. The main novelty is the cheap and accurate calculation of the shape gradients, using adjoint methods, which allows optimization with gradient-based algorithms. This is useful in two complementary ways. Firstly, these algorithms quickly converge to shapes that a human designer, using physical insight and trial and error, would probably not consider. Secondly, the adjoint methods provide physical insight into

the mechanisms that influence the objective functions. It can be then used to alter the choice of shape parameters if it becomes apparent that the algorithm is missing a good shape due to a bad choice of shape parameters. The method in this paper is general and could be applied to many different applications in microfluidics. Its main requirements are that the steady flow Mach number and oscillating flow Mach number are small, and that dissipation is dominated by thermoviscous mechanisms.

Now that the technique has been proven on a 2-D geometry, the desirable next step is to apply it to 3-D geometries. For the adjoint methods and optimization algorithms, the extension from two to three dimensions is straightforward. For the shape parametrization, this extension is usually harder. In this case, however, the manufacturable 3-D shapes of inkjet print heads are severely constrained because they are etched into silicon wafers. Similar constraints apply to many microfluidic applications. These constraints, which require geometries to be close to two-dimensional, both render the 2-D analysis more relevant and make the 3-D shape parametrization more simple. Another extension, which is particularly relevant to inkjet printing, is to consider non-Newtonian fluids. Although these are challenging to model, it should be relatively straightforward to develop adjoints of these models. Another extension, which is the subject of our current work, is to use adjoint methods to optimize the droplet formation stage by varying the signal applied to the piezo-electric actuator.

Acknowledgements

We gratefully acknowledge the European Union’s Framework Programme for Research and Innovation Horizon 2020 under the Marie Skłodowska-Curie Innovative Training Programme, H2020-MSCA-ITN-2015, for funding this project.

Appendix A

A.1. Derivation of the thermoviscous acoustic adjoint equations

The thermoviscous acoustic eigenvalue problem (2.20) can be written in terms of the velocity, pressure and temperature $\hat{\mathbf{q}}^T = (\hat{u}_i, \hat{P}, \hat{T})$ eigenvector and the complex eigenvalue s in matrix form $sA\hat{\mathbf{q}} + B\hat{\mathbf{q}} = 0$:

$$s \begin{bmatrix} 1 & 0 & 0 \\ 0 & \gamma & -1 \\ 0 & -1 & \frac{1}{\gamma - 1} \end{bmatrix} \hat{\mathbf{q}} + \begin{bmatrix} -\tilde{R}e^{-1} \nabla_j \hat{\tau}_{ij} & \nabla_i & 0 \\ \nabla_i & 0 & 0 \\ 0 & 0 & -\frac{1}{(\gamma - 1)\tilde{P}e} \Delta \end{bmatrix} \hat{\mathbf{q}} = 0, \quad (A 1)$$

where $\hat{\tau}_{ij}$ denotes the viscous stress tensor differential operator, $\hat{\tau}_{ij}\hat{u} \equiv \hat{\tau}_{ij}$. The direct boundary conditions $\mathcal{N}\hat{\mathbf{q}} = 0$ satisfy the following equations:

$$Z(s, x)\hat{u}_i = (-\hat{P}\delta_{ij} + \tilde{R}e^{-1}\hat{\tau}_{ij})n_j, \quad (A 2a)$$

$$\hat{T} = -\alpha_w(s, x)\frac{\partial \hat{T}}{\partial n}. \quad (A 2b)$$

There exists a corresponding adjoint state vector $\mathbf{q}^+ = (u_i^+, P^+, T^+)$. We define the following volume and surface inner products:

$$\langle \mathbf{a}, \mathbf{b} \rangle = \int_{\Omega} \mathbf{a}^* \mathbf{b} \, dx, \quad (A 3a)$$

$$\langle \mathbf{a}, \mathbf{b} \rangle = \int_{\partial\Omega} \mathbf{a}^* \mathbf{b} \, ds. \tag{A 3b}$$

A Lagrangian functional of the system (A 1) with a objective function \mathcal{J} is defined as

$$\mathcal{L} = \mathcal{J} - \langle \mathbf{q}^+, s\hat{\mathbf{q}} + B\hat{\mathbf{q}} \rangle. \tag{A 4}$$

The system’s eigenvalue sensitivity can be determined by setting $\mathcal{J} = s$.

The optimality condition yields that the total variation of the Lagrangian with respect to the direct $\hat{\mathbf{q}}$, s , and the adjoint \mathbf{q}^+ variables must be zero. The variation with respect to the adjoint variables gives the direct state equations. To determine the adjoint set of equations, we take the variation with respect to the direct variables and integrate the volume term in (A 4) by parts:

$$\frac{\partial \mathcal{L}}{\partial \hat{\mathbf{q}}} \delta \hat{\mathbf{q}} = 0 = \frac{\partial \mathcal{J}}{\partial \hat{\mathbf{q}}} \delta \hat{\mathbf{q}} - \langle s^* A^+ \mathbf{q}^+ + B^+ \mathbf{q}^+, \delta \hat{\mathbf{q}} \rangle - \{ \mathcal{N}^+ \mathbf{q}^+, \delta \hat{\mathbf{q}} \}. \tag{A 5}$$

The volume terms define the adjoint state equations, which in matrix form are:

$$s^* \begin{bmatrix} 1 & 0 & 0 \\ 0 & \gamma & -1 \\ 0 & -1 & \frac{1}{\gamma - 1} \end{bmatrix} \mathbf{q}^+ + \begin{bmatrix} -\tilde{R}e^{-1} \nabla_j \hat{\boldsymbol{\tau}}_{ij} & -\nabla_i & 0 \\ -\nabla_i & 0 & 0 \\ 0 & 0 & -\frac{1}{(\gamma - 1)\tilde{P}e} \Delta \end{bmatrix} \mathbf{q}^+ = 0, \tag{A 6}$$

where $\hat{\boldsymbol{\tau}}_{ij} \mathbf{q}^+ = \tau_{ij}^+ \equiv \nabla_j u_i^+ + \nabla_i u_j^+ - 2/3 \delta_{ij} \operatorname{div} u^+$ is the adjoint viscous stress tensor. The surface terms determine the adjoint boundary conditions $\mathcal{N}^+ \mathbf{q}^+ = 0$:

$$Z^*(s, x) u_i^+ = (P^+ \delta_{ij} + \tilde{R}e^{-1} \tau_{ij}^+) n_j, \tag{A 7a}$$

$$T^+ = -\alpha_w(s, x) \frac{\partial T^+}{\partial n}. \tag{A 7b}$$

Consideration of the direct (A 1) and adjoint (A 6) state equations, and the corresponding boundary conditions (A 2), (A 7) yields that the adjoint state can be expressed in terms of the direct state variables:

$$\mathbf{q}^+ = (-\hat{u}_i^*, \hat{P}^*, \hat{T}^*). \tag{A 8}$$

The variation of the Lagrangian with respect to the eigenvalue δs gives the normalization condition:

$$\frac{\partial \mathcal{L}}{\partial s} \delta s = 0 = \delta s - \langle \mathbf{q}^+, A\hat{\mathbf{q}} \rangle \delta s - \left\langle \mathbf{q}^+, \frac{\partial \mathcal{N}}{\partial s} \hat{\mathbf{q}} \right\rangle \delta s. \tag{A 9}$$

Taking into account the adjoint state representation in terms of the direct variables, the normalization condition is:

$$1 = -\langle \hat{u}_i^*, \hat{u}_i \rangle + \langle \hat{P}^*, \gamma \hat{P} - \hat{T} \rangle + \left\langle \hat{T}^*, \frac{\hat{T}}{\gamma - 1} - \hat{P} \right\rangle + \left\langle \hat{u}_i^*, \frac{\partial Z}{\partial s} \hat{u}_i \right\rangle - \left\langle \frac{\partial \hat{T}^*}{\partial n}, \frac{(\partial \alpha_w / \partial s) \partial \hat{T}}{(\gamma - 1)\tilde{P}e \partial n} \right\rangle. \tag{A 10}$$

If the boundaries’ impedance and thermal accommodation coefficient are frequency independent, the surface terms in (A 10) vanish and the normalization condition is given by

$$\langle \mathbf{q}^+, A\hat{\mathbf{q}} \rangle = 1. \tag{A 11}$$

A.2. Oscillating flow shape sensitivity

We want to construct the eigenvalue shape sensitivity $G(\hat{\mathbf{q}}, \mathbf{q}^+)$ of the thermoviscous acoustic problem for a given shape displacement field V . We take the variation of the Lagrangian (A 4) with respect to a shape perturbation $\mathcal{L}'[V]$, and, due to the choice of the adjoint state (A 8), only the boundary terms do not vanish. This gives us the shape gradient

$$\begin{aligned} \mathcal{L}'[V] = & -\{\mathcal{N}^+ \mathbf{q}^+, \hat{\mathbf{q}}'[V]\} = \{u_i^+, (-\hat{P}'[V]\delta_{ij} + \tilde{R}e^{-1} \hat{\tau}'_{ij}[V])n_j\} \\ & - \{(P^+ \delta_{ij} + \tilde{R}e^{-1} \tau_{ij}^+)n_j, \hat{u}'_i[V]\} \\ & + \left\{ T^+, \frac{1}{(\gamma - 1)\tilde{P}e} \frac{\partial \hat{T}'[V]}{\partial n} \right\} - \left\{ \frac{\partial T^+}{\partial n}, \frac{1}{(\gamma - 1)\tilde{P}e} \hat{T}'[V] \right\}. \end{aligned} \quad (\text{A } 12)$$

For simplicity, we introduce the direct $\hat{\sigma}_{ij} = -\hat{P}\delta_{ij} + \tilde{R}e^{-1} \hat{\tau}_{ij}$ and the adjoint $\sigma_{ij}^+ = -P^+ \delta_{ij} + \tilde{R}e^{-1} \tau_{ij}^+$ force tensors. Also, we define the direct $\hat{q}_i = (1/(\gamma - 1)\tilde{P}e)\nabla_i \hat{T}$ and adjoint $q_i^+ = (1/(\gamma - 1)\tilde{P}e)\nabla_i T^+$ heat fluxes, and their normal components $\hat{q}_i n_i \equiv \hat{q}_n$, $q_i^+ n_i \equiv q_n^+$.

On boundaries, the conditions (A 2) hold, resulting in the compliant and thermal boundary shape derivatives:

$$\begin{aligned} 0 = d(Z\hat{u}_i - \hat{\sigma}_{ij}n_j)[V] & = dZ[V]\hat{u}_i + Z d\hat{u}_i[V] - d\hat{\sigma}_{ij}[V]n_j - \hat{\sigma}_{ij} dn_j[V], \quad (\text{A } 13a) \\ 0 = d\left(\hat{T} + \alpha_w \frac{\partial \hat{T}}{\partial n}\right)[V] & = d\hat{T}[V] + d\alpha_w[V] \frac{\partial \hat{T}}{\partial n} + \alpha_w dn_j[V]\nabla_j \hat{T} + \alpha_w \frac{\partial d\hat{T}[V]}{\partial n}. \end{aligned} \quad (\text{A } 13b)$$

As discussed in § 3.1, the total and the local shape derivatives of the Dirichlet and Neumann boundaries, satisfy:

$$\begin{aligned} d\hat{u}_i[V] & = \hat{u}'_i[V] + (V \cdot \nabla)\hat{u}_i, \quad (\text{A } 14a) \\ d\hat{\sigma}_{ij}[V] & = \hat{\sigma}'_{ij}[V] + (V \cdot \nabla)\hat{\sigma}_{ij}, \quad (\text{A } 14b) \\ d\hat{T}[V] & = \hat{T}'[V] + (V \cdot \nabla)\hat{T}, \quad (\text{A } 14c) \\ d(\nabla_j \hat{T})[V] & = \nabla_j \hat{T}'[V] + (V \cdot \nabla)\nabla_j \hat{T}. \quad (\text{A } 14d) \end{aligned}$$

Assuming the boundary properties (impedance and thermal accommodation) to be constant in the displacement direction, the material derivative results in $dZ[V] = 0$, $d\alpha_w[V] = 0$.

The displacement vector field V can be presented as a sum of its normal and tangential components, $V = (V \cdot \mathbf{n})\mathbf{n} + \sum_{i=1}^{d-1} (V \cdot \boldsymbol{\tau}_i)\boldsymbol{\tau}_i$, where $\boldsymbol{\tau}_i$ spans the $(d - 1)$ -dimensional space tangent to the surface. As shown in Sokolowski & Zolesio (1992), a shape derivative vanishes in the tangential direction, since any boundary deformation in the tangential direction does not change the domain boundary. Therefore, for a domain boundary of sufficient smoothness the shape derivatives in the direction of the displacement field are equivalent to the shape derivatives in its normal projection. Therefore V can be replaced with $(V \cdot \mathbf{n})\mathbf{n}$ and $(V \cdot \nabla)$ with $(V \cdot \mathbf{n})\partial/\partial \mathbf{n}$. By introducing the tangential gradient $\nabla_i^\Gamma = \nabla_i - n_i n_j \nabla_j$, the shape derivative of the boundary normal is (Sonntag, Schmidt & Gauger 2016)

$$dn_i[V] = -\nabla_i^\Gamma (V \cdot \mathbf{n}). \quad (\text{A } 15)$$

Combining (A 13)–(A 15), the shape derivatives of the compliant boundary condition and the thermal boundary condition result in

$$Z\hat{u}'_i[V] - \hat{\sigma}'_{ij}[V]n_j = -Z(V \cdot \mathbf{n}) \frac{\partial \hat{u}_i}{\partial n} + (V \cdot \mathbf{n})n_j \frac{\partial \hat{\sigma}_{ij}}{\partial n} - \hat{\sigma}_{ij} \nabla_i^\Gamma (V \cdot \mathbf{n}), \quad (\text{A } 16a)$$

$$\hat{T}'[V] + \alpha_w \frac{\partial \hat{T}'[V]}{\partial n} = -(V \cdot \mathbf{n}) \frac{\partial \hat{T}}{\partial n} - \alpha_w (V \cdot \mathbf{n})n_j \frac{\partial \nabla_j \hat{T}}{\partial n} + \alpha_w \nabla_i^\Gamma (V \cdot \mathbf{n}) \nabla_i \hat{T}. \quad (\text{A } 16b)$$

Considering the adjoint boundary conditions (A 7) in the primal shape derivative (A 12) and substituting the above expressions, we obtain

$$\mathcal{L}'[V] = \{u_i^+, \hat{\sigma}'_{ij}[V]n_j - Z\hat{u}'_i[V]\} - \left\{ q_n^+, \hat{T}'[V] + \alpha_w \frac{\partial \hat{T}'[V]}{\partial n} \right\} \quad (\text{A } 17a)$$

$$= \left\{ u_i^+, (V \cdot \mathbf{n}) \left(Z \frac{\partial \hat{u}_i}{\partial n} - n_j \frac{\partial \hat{\sigma}_{ij}}{\partial n} \right) + \hat{\sigma}_{ij} \nabla_j^\Gamma (V \cdot \mathbf{n}) \right\} + \left\{ q_n^+, (V \cdot \mathbf{n}) \left(\frac{\partial \hat{T}}{\partial n} + \alpha_w n_j \frac{\partial \nabla_j \hat{T}}{\partial n} \right) - \alpha_w \nabla_i^\Gamma (V \cdot \mathbf{n}) \nabla_i \hat{T} \right\}. \quad (\text{A } 17b)$$

The shape gradient is represented by stress and thermal contributions. Two terms are still not in Hadamard form, so we apply the surface tangential Green’s formula (Delfour & Zolésio 2011). The relation holds for a smooth vector field A and a scalar field b :

$$\int_{\partial\Omega} (A, \nabla^\Gamma) b \, ds = \int_{\partial\Omega} \kappa b(A, n) - b \operatorname{div}^\Gamma A \, ds. \quad (\text{A } 18)$$

Here $\kappa = \operatorname{div}^\Gamma n$ describes the surface curvature. With $A_j = -u_i^{+*} \hat{\sigma}_{ij}$, $b = (V \cdot \mathbf{n})$, the transformation of the stress contribution (the first surface integral in (A 17b)) to Hadamard form is given by

$$u_i^{+*} \hat{\sigma}_{ij} \nabla_j^\Gamma (V \cdot \mathbf{n}) = \kappa (V \cdot \mathbf{n}) u_i^{+*} \hat{\sigma}_{ij} n_j - (V \cdot \mathbf{n}) \nabla_j^\Gamma (u_i^{+*} \hat{\sigma}_{ij}), \quad (\text{A } 19)$$

and using the definition of the tangential gradient, the tangential divergence in (A 19) combines with the following term and we obtain:

$$\nabla_j^\Gamma (u_i^{+*} \hat{\sigma}_{ij}) + u_i^{+*} n_j \frac{\partial \hat{\sigma}_{ij}}{\partial n} = \nabla_j (u_i^{+*} \hat{\sigma}_{ij}) - \frac{\partial u_i^{+*}}{\partial n} n_j \hat{\sigma}_{ij}. \quad (\text{A } 20)$$

For the thermal contribution (the second surface integral in (A 17b)) $A_j = \alpha_w \nabla_j \hat{T} (\partial T^+ / \partial n)^*$ so the Hadamard form is:

$$\begin{aligned} & \alpha_w q_n^+ \nabla_j \hat{T} \nabla_j^\Gamma (V \cdot \mathbf{n}) \\ &= \kappa (V \cdot \mathbf{n}) \alpha_w q_n^{+*} \frac{\partial \hat{T}}{\partial n} - (V \cdot \mathbf{n}) \nabla_j^\Gamma (\alpha_w q_n^{+*} \nabla_j \hat{T}) \\ &= (V \cdot \mathbf{n}) \left(\kappa \alpha_w q_n^{+*} \frac{\partial \hat{T}}{\partial n} - \alpha_w q_n^{+*} \left(\Delta \hat{T} - n_j \frac{\partial \nabla_j \hat{T}}{\partial n} \right) - \nabla_j^\Gamma (\alpha_w q_n^{+*}) \nabla_j \hat{T} \right). \quad (\text{A } 21) \end{aligned}$$

After rearranging the terms in (A 17), the shape derivative in Hadamard form is given by the surface integral of the normal displacement and the sum of the stress and thermal sensitivity functionals, G_s^{str} and G_s^{th} :

$$s'[V] = \mathcal{L}'[V] = \int_{\partial\Omega} (V \cdot \mathbf{n})(G_s^{str}(\hat{\mathbf{q}}, \mathbf{q}^+) + G_s^{th}(\hat{\mathbf{q}}, \mathbf{q}^+)), \quad (\text{A } 22)$$

where the functionals are defined as

$$G_s^{str}(\hat{\mathbf{q}}, \mathbf{q}^+) = \frac{\partial \hat{u}_i}{\partial n} n_j \sigma_{ij}^{+*} + \frac{\partial u_i^{+*}}{\partial n} n_j \hat{\sigma}_{ij} + \kappa \hat{u}_i \sigma_{ij}^{+*} n_j - \nabla_j (u_i^{+*} \hat{\sigma}_{ij}), \quad (\text{A } 23a)$$

$$G_s^{th}(\hat{\mathbf{q}}, \mathbf{q}^+) = \frac{\partial \hat{T}}{\partial n} q_n^{+*} + \frac{\partial T^{+*}}{\partial n} \hat{q}_n + \kappa \hat{T} q_n^{+*} - \nabla_j (T^{+*} \hat{q}_j). \quad (\text{A } 23b)$$

Finally, considering (A 8), the eigenvalue sensitivity functionals can be derived:

$$\left. \begin{aligned} G_s^{str} &= - \left(2 \frac{\partial \hat{u}_i}{\partial n} n_j \hat{\sigma}_{ij} + \kappa \hat{u}_i \hat{\sigma}_{ij} n_j - \nabla_j (\hat{u}_i \hat{\sigma}_{ij}) \right), \\ G_s^{th} &= 2 \frac{\partial \hat{T}}{\partial n} \hat{q}_n + \kappa \hat{T} \hat{q}_n - \nabla_j (\hat{T} \hat{q}_j). \end{aligned} \right\} \quad (\text{A } 24)$$

Two special cases, the no-slip and stress-free boundaries, simplify the viscous sensitivity functional to

$$G_{s,nsl}^{str} = - \frac{\partial \hat{u}_i}{\partial n} n_j \hat{\sigma}_{ij}, \quad (\text{A } 25a)$$

$$G_{s,free}^{str} = \nabla_j (\hat{u}_i \hat{\sigma}_{ij}), \quad (\text{A } 25b)$$

and the thermal sensitivity functional turns into the following expressions on isothermal and adiabatic boundaries:

$$G_{s,iso}^{th} = \frac{\partial \hat{T}}{\partial n} \hat{q}_n, \quad (\text{A } 26a)$$

$$G_{s,ad}^{th} = - \nabla_j (\hat{T} \hat{q}_j). \quad (\text{A } 26b)$$

REFERENCES

- BELTMAN, W. M. 1998 Viscothermal wave propagation including acousto-elastic interaction. PhD thesis, University of Twente, The Netherlands.
- BELTMAN, W. M. 1999 Viscothermal wave propagation including acousto-elastic interaction. Part I. Theory. *J. Sound Vib.* **227** (3), 555–586.
- BERGGREN, M., BERNLAND, A. & NORELAND, D. 2018 Acoustic boundary layers as boundary conditions. *J. Comput. Phys.* **371**, 633–650.
- BOGY, D. B. & TALKE, F. E. 1984 Experimental and theoretical study of wave propagation phenomena in drop-on-demand ink jet devices. *IBM J. Res. Dev.* **28** (3), 314–321.
- CARSLAW, H. S. & JAEGER, J. C. 1986 *Conduction of Heat in Solids*. Clarendon Press.
- CHRISTENSEN, R. 2017 Topology optimization of thermoviscous acoustics in tubes and slits with hearing aid applications. In *COMSOL Conference 2017 Rotterdam, at Rotterdam*. COMSOL.
- CHU, B. T. 1965 On the energy transfer to small disturbances in fluid flow (part I). *Acta Mechanica* **1** (3), 215–234.

- CULICK, F., HEITOR, M. V. & WHITELAW, J. H. 2012 Equations for unsteady motions in combustion chambers. In *Unsteady Combustion*, vol. 306. chap. 3, Springer Science & Business Media, 3-1-3-14.
- DELFOUR, M. & ZOLÉSIO, J. 2011 Shape and tangential differential calculus. In *Shapes and Geometries*, 2nd edn. chap. 9, pp. 457-518. Society for Industrial and Applied Mathematics.
- GEUZAINÉ, C. & REMACLE, J.-F. 2009 Gmsh: a 3D finite element mesh generator with built-in pre- and post-processing facilities. *Intl J. Numer. Meth. Engng* **79** (11), 1309-1331.
- GUNZBURGER, M. 2002 *Perspectives in Flow Control and Optimization*. Society for Industrial and Applied Mathematics.
- HOATH, S. D. (Ed.) 2016 *Fundamentals of Inkjet Printing*, Wiley-VCH Verlag GmbH & Co. KGaA.
- HOMENTCOVSCHI, D., MILES, R. N., LOEPPERT, P. V. & ZUCKERWAR, A. J. 2014 A microacoustic analysis including viscosity and thermal conductivity to model the effect of the protective cap on the acoustic response of a MEMS microphone. *Microsystem Technol.* **20** (2), 265-272.
- HOMENTCOVSCHI, D., MURRAY, B. T. & MILES, R. N. 2010 An analytical formula and FEM simulations for the viscous damping of a periodic perforated MEMS microstructure outside the lubrication approximation. *Microfluid. Nanofluid.* **9** (4-5), 865-879.
- KAMPINGA, W. R., WIJNANT, Y. H. & DE BOER, A. 2010 Performance of several viscothermal acoustic finite elements. *Acta Acust. united Acust.* **96**, 115-124.
- KAMPINGA, W. R., WIJNANT, Y. H. & DE BOER, A. 2011 An efficient finite element model for viscothermal acoustics. *Acta Acust. united Acust.* **97** (4), 618-631.
- LOGG, A., MARDAL, K.-A. & WELLS, G. N. 2012 *Automated Solution of Differential Equations by the Finite Element Method*. Springer.
- LUCHINI, P. & BOTTARO, A. 2014 Adjoint equations in stability analysis. *Annu. Rev. Fluid Mech.* **46**, 493-517.
- MOSER, M. 1980 Damping of structure-borne sound by the viscosity of a layer between 2 plates. *Acustica* **46** (2), 210-217.
- MÜLLER, B. 1998 Low-Mach-number asymptotics of the Navier-Stokes equations. *J. Engng Maths* **34** (1), 97-109.
- MYERS, M. K. 1980 On the acoustic boundary condition in the presence of flow. *J. Sound Vib.* **71** (3), 429-434.
- RIENSTRA, S. W. & HIRSCHBERG, A. 2013 An introduction to acoustics. *Eindhoven University of Technology*.
- ROGNES, M. E. & LOGG, A. 2013 Automated goal-oriented error control I: stationary variational problems. *SIAM J. Sci. Comput.* **35** (3), C173-C193.
- SAMAREH, J. A. 2001 Survey of shape parameterization techniques for high-fidelity multidisciplinary shape optimization. *AIAA J.* **39** (5), 877-884.
- SCHMIDT, S. & SCHULZ, V. 2010 Shape derivatives for general objective functions and the incompressible Navier-Stokes equations. *Control Cybern.* **39** (3), 677-713.
- SECCOMBE, D. *et al.* 1997 Ink-cooled thermal inkjet printhead. US Patent 5657061.
- SOKOLOWSKI, J. & ZOLESIO, J.-P. 1992 *Introduction to Shape Optimization*. Springer.
- SONNTAG, M., SCHMIDT, S. & GAUGER, N. R. 2016 Shape derivatives for the compressible Navier-Stokes equations in variational form. *J. Comput. Appl. Maths* **296**, 334-351.
- SVANBERG, K. 1987 The method of moving asymptotes - a new method for structural optimization. *Intl J. Numer. Meth. Engng* **24** (2), 359-373.
- TIJDEMAN, H. 1975 On the propagation of sound waves in cylindrical tubes. *J. Sound Vib.* **39** (1), 1-33.